Tailoring α-alumina powder morphology through spray drying for cold consolidation by binder jetting

Marco Mariani [a,*], Guillermo Frias Blanco [b], Elisa Mercadelli [c], Antonio Javier Sánchez-Herencia [b], Carmen Galassi [a,c], Nora Lecis [a], Begoña Ferrari [b]

[a] Department of Mechanical Engineering, Politecnico di Milano, via La Masa 1, Milano, 20156, Italy
[b] Instituto de Cerámica y Vidrio (ICV), CSIC; C/Kelsen 5, Madrid, 28049, Spain
[c] Istituto di Scienza e Tecnologia dei Materiali Ceramici, CNR-ISTEC, Via Granarolo 64, Faenza, 48018, Italy

ARTICLE INFO

ABSTRACT

Our work describes an optimised procedure for granulating nanometric and fine micrometric particles by spray-drying to achieve ready-to-print α-Al$_2$O$_3$ powders. The study started by identifying raw materials suited for the process through complete characterisation of particles shape, size, and surface properties. Then, dispersion in diluted and concentrated water-based suspensions was achieved thanks to polyethyleneimine and the effect of gradual dispersant addition was assessed by determining ζ potential and aggregates size variation. Suspensions rheology was studied and modelled through Krieger-Dougherty equation to identify the maximum solid loading allowing sufficient feeding through the spray-dryer nozzle. Finally, optimisation of the granulation conditions was performed.

The procedure has allowed to achieve size distributions with D$_{90}$ < 50 μm and Hausner ratio <1.3 ensuring sufficient flowability. The granulated powders were printed and the porosity evolution of the samples after sintering was studied by mercury intrusion porosimetry and SEM analysis.

1. Introduction

Additive manufacturing (AM) of ceramic materials offers unique advantages over conventional manufacturing, namely high degree of design freedom, reduced material waste and short production times [1]. Nevertheless, the commercialisation of these solutions is still extremely limited for the many issues that must be faced when dealing with materials featuring extremely high melting points and processing-dependent functional properties, as in the case of ceramics [2]. These factors have pushed for the wider adoption of indirect over direct AM techniques: indeed, splitting the shaping phase from the sintering process allows to achieve application-oriented designs more easily and then to obtain the desired microstructure through specific thermal treatments [3,4]. Among these techniques, the most important are Stereolithography (SLA) [5–7], Material Extrusion (e.g. Fused Deposition Modeling) [8–10], Robocasting/Direct Ink Writing (DIW) [11–13]) and Binder Jetting (BJ) [14–17].

Each of them offers specific advantages, however they all suffer from the need of a specific kind of feedstock. Indeed, conventional raw materials cannot be employed directly in these productions, but they need to be pre-processed accordingly to the requirements: photocurable colloidal suspensions for SLA, ceramic-loaded thermoplastic filaments for material thermal extrusion, ceramic pastes/inks for robocasting and DIW, and ceramic powders for BJ. BJ is based on the selective deposition of a liquid binder on a powder bed, obtained through layer-by-layer spreading of dry particles. The final properties of the printed components are strictly dependent on the packing density and porosity distribution of the powder bed [18].

Optimisation of the packing behaviour is achieved with well-flowing spherical granules with a wide size distribution or possibly with a multimodal distribution, while reduced pore volume with a minimal channel diameter is obtained by employing fine particles [19]. In addition, the printed component should also provide an excellent sinterability to achieve full densification, which is dependent on the primary particles size. Generally technical ceramic particles, both in lab synthesised or commercial, are extremely fine (in the nanometric range), so their large specific surface area (SSA) enhances diffusion mechanisms during sintering. However, their flowability is extremely

Table 1

Composition and nomenclature (A/B for Almatis CT1200SG/Bitossi powder, 30/35 for solid loading, I/G for binder type, L/S for nozzle size, HT for high inlet temperature) of the high solid loading suspensions for spray drying and main granulation setup parameters.

Name	Powder		Dispersant		Binder		d_{nozzle}	T_{inlet}
	Type	vol%	Type	wt.%	Type	wt.%	mm	°C
A30I2L	CT1200SG	30	PEI	0.5	PEI	2.0	1	205
A30G2L	CT1200SG	30	PEI	0.5	PEG	2.0	1	205
A30I2S	CT1200SG	30	PEI	0.5	PEI	2.0	0.5	205
A35G1L	CT1200SG	35	PEI	0.5	PEG	1.0	1	205
A35I2S	CT1200SG	35	PEI	0.5	PEI	2.0	0.5	205
A30I2SHT	CT1200SG	30	PEI	0.5	PEI	2.0	0.5	250
B30I2S	BITOSSI	30	PEI	0.5	PEI	2.0	0.5	205

limited, thus their packing density is poor [20]. On the contrary, ready-to-press powders obtained by granulation feature optimal sphericity and flowability, but their average diameter is normally in the ~50–150 μm range, therefore generating large pores that are challenging to fill during pressureless sintering [21,22]. A third choice consists of spherical dense particles in the micrometric range obtained by gas or liquid atomisation from melt ceramic [14]. Although the obtained green density may be excellent, the SSA is extremely reduced, thus hindering densification, and not all ceramic powders can be processed with this technique.

Our work is aimed at presenting a systematic approach for granulating fine and spherical powder through spray drying technique to achieve an optimal compromise among the aforementioned requirements for BJ. The investigation is focused on both colloidal suspension preparation and granulation processing for water stable materials (α-alumina) to provide a comprehensive procedure for the production of ready-to-print powders. The prepared materials are then investigated in the actual printing process to determine which granule features are most influential to achieve successful densification and optimal geometrical accuracy.

2. Materials and methods

2.1. Materials

Three different feedstock materials were selected for this study: α-Al$_2$O$_3$ CT1200SG and CT530SG from Almatis GmbH (Germany) and α-Al$_2$O$_3$ (a batch of fine particles) from Industrie Bitossi SpA (Italy). The latter is a "waste" material obtained by sieving the ultrafine fraction from a granulated powder, so it could present minimal traces of organic material. Low and high solid loading suspensions were prepared by mixing powder, deionized water, polyethyleneimine (PEI, MW 25.000, Sigma Aldrich, Germany), as dispersant and binder, and polyethylene glycol (PEG 400, Sigma Aldrich, Germany) as binder. The pH of the suspensions was corrected by adding either tetramethylammonium hydroxide (TMAH) for pH > 8 and nitric acid (HNO$_3$) for pH < 6. Diluted suspensions were prepared by mechanical stirring, while concentrated ones were obtained by ball milling with alumina balls (5 mm diameter) as milling media, setting at 1:1:1 the balls-to-suspension-to-air volume ratio. The milling was set to last 60 min with a rotation speed of 350 rpm (G90 Jar Mill, Gladstone Engineering Co Ltd., UK).

2.2. Granulating conditions

Selected suspensions were granulated by spray drying. Alumina-based suspensions were prepared with 30/35 vol% solid loading, 0.5 wt% of dispersant (PEI) with respect to solid and 1.0/2.0 wt% of binder (PEI/PEG) with respect to solid. All the details for the suspensions composition and spray drying parameters are summarised in Table 1.

The granulation was performed with a two-fluid nozzle (top feed and co-current mode) atomizer with an internal diameter of 0.5 mm for suspensions A30I2S, A35I2S, A30I2SHT, B30I2S and 1 mm for A30I2L,

Table 2

Operating conditions of rheological measurement under control shear rate (CR) and control shear stress (CS) modes.

Mode	Phase	t_{start}	t_{end}	γ'_{start}	γ'_{end}	τ_{start}	τ_{end}
		s	s	s^{-1}	s^{-1}	mPa	mPa
CR	1	0	180	0	1000	–	–
	2	180	240	1000	1000	–	–
	3	240	420	1000	0	–	–
CS	1	0	120	–	–	0	threshold[a]
	2	120	240	–	–	threshold[a]	0

[a] Threshold values selected from the shear stress curves of each suspension obtained in CR conditions with 150 s^{-1} < γ' < 200 s^{-1} during phase 3.

A30G2L, A35G1L and compressed air at 1.2 bar pressure. The flow rate was constant at 15 mL min^{-1} or slightly adjusted if necessary, to allow droplets formation and avoid nozzle clogging. The particle collector featured a cyclone configuration. The temperatures at the inlet and outlet regions were set at 205 °C and 140 °C respectively, with the exception of A30I2SHT case that featured 250 °C and 160 °C.

2.3. Characterisation of the dry powders and suspensions

All the initial materials and granulated powders were characterised in terms of volume-based particle size distribution (PSD$_V$) by means of laser diffraction (Mastersizer S granulometer, Malvern Instruments Ldt., UK) and number-based particle size distribution (PSD$_N$) by static image technique (Morphologi 4 granulometer, Malvern Instruments Ltd., UK). The latter instrument was also employed to assess the shape regularity of the detected particles, which is represented by the "circularity" factor calculated as the ratio between the length of the inscribed circle and the actual length of the section perimeter (1 = perfect circle, 0 = perfect fiber). The specific surface area (SSA) of the raw materials was measured by N$_2$ adsorption analyses (Monosorb Surface Area picnometer, Quantachrome Corporation, USA). Particles shape and aspect of raw materials and granulated powders were inspected by FE-SEM (Sigma 500 microscope, ZEISS GmbH, Germany) and by SEM (TM1000 microscope, Hitachi, Japan).

The surface charge of the starting particles in water suspensions at 1 gL^{-1} concentration (with KCl 10^{-2} M to maintain a constant ionic strength) at varying pH (from 4 to 12) was assessed by ζ potential measurement (Zetasizer Nano ZS, Malvern Instruments Ltd., UK). The same measurements were repeated after addition of PEI as dispersant at different concentrations (0.1/0.2/0.3/0.5/1.0/1.5/2.5/5.0 wt%). For Al$_2$O$_3$ CT1200SG only, the measurements were performed with PEI concentrations 0.3/0.5/0.8/1.0 wt%. This set of analyses allowed to evaluate the behaviour and the aggregation state of the materials at all the stages of suspension preparation.

The rheological properties of alumina slurries were assessed in control shear rate γ' (CR) and control shear stress τ (CS) testing conditions at room temperature with a double-cone plate fixture of 60 mm of diameter and an angle of 2° (Haake Mars 60 rheometer, Thermo Scientific, Germany). The details of the testing conditions are provided in
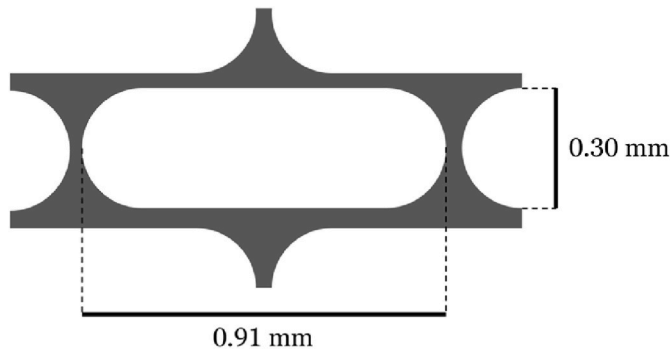
Fig. 1. Unit cell of the "V5" sieve for dispensing rate measurements.

Table 2. The values of viscosity measured under CS testing at $\gamma' = 100$ s^{-1} for suspensions with a progressively lower solid loading were employed in a Krieger-Dougherty model [23,24], to identify the suspension composition with the highest solid loading and a suitable viscosity for nozzle feeding, according to Eq. (1):

$$\eta_{100s^{-1}} = \eta_{medium}\left(1 - \frac{\Phi_{vol}}{\Phi_{vol,max}}\right)^{-\Phi_{vol,max}[n]} \tag{1}$$

where η_{100s}^{-1} is the suspension viscosity measured at $\gamma' = 100$ s^{-1}, η_{medium} is a parameter accounting for the viscosity of the liquid medium (water in this case), Φ_{vol} is the volume fraction of the solid in the suspension, $\Phi_{vol,max}$ is the maximum volume fraction of the solid, that can be identified with the maximum packing degree that can be achieved using a dispersed and stabilised suspension, and *[n]* is a shape factor associated to the solid particle features.

Suspension was granulated using a spray-drier (NIRO® MOBILE MINOR granulometer, GEA, Germany) with interchangeable nozzles of 0.5 and 1 mm in diameter. The granulation process efficiency was evaluated from the mass yield, calculated as in Eq. (2):

$$Yield = \frac{m_{start} - m_{end}}{m_{start}} 100 \tag{2}$$

where m_{start} is the mass of the raw material added to the suspension and m_{end} is the mass of the collected granulated powder.

Finally, the flowability of the obtained powder was evaluated by considering the apparent and tapped density, referred to as ρ_{app} and ρ_{tap}, being the theoretical density of α-Al$_2$O$_3$ 3.94 g cm^{-3}. These values were employed to calculate the Hausner ratio (*HR*) from Eq. (3) [25]:

$$HR = \frac{\rho_{tap}}{\rho_{app}} \tag{3}$$

A second method was also employed to evaluate the flowability of powders, since the previous technique does not mimic well the deposition mode occurring during the printing process. In this case, the average mass flow of the powders through the powder hopper sieve of the printer was collected and measured to determine the dispensing rate. As per the authors knowledge, a similar quantification of the powder flow was performed only by Oropeza et al. with a customized printer setup [26]; however this is the first time it is employed to evaluate and compare the flowing behaviour of different feedstocks. The material was flowed five times through a 10 × 20 mm^2 section of the "V5" sieve (details in Fig. 1) provided with the binder jetting printer with an above column height of 70 mm. The ultrasonic vibration of the powder dispenser was activated for 10 s at a frequency of 37 kHz.

2.4. Printing and densification

A30I2L, A30I2S, A35I2S, A30I2SHT and B30I2S granulated powders were employed as feedstock materials to produce rectangular cuboid
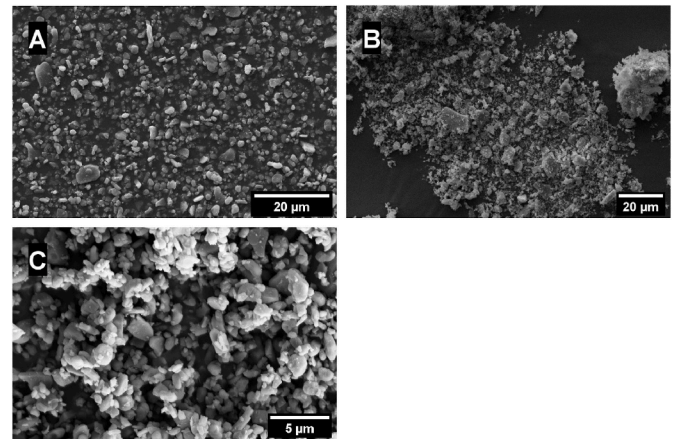

Fig. 2. SEM images of: A) CT1200SG; B) CT530SG; C) BITOSSI powder at different magnification levels.

components ($l_x = 6$ mm; $l_y = 8$ mm; $l_z = 4$ mm) without internal empty cavities by the binder jetting printer (Innovent+ 3D printer, ExOne, US). The powder deposition and spreading parameters were optimised for each feedstock, while the layer thickness and binder saturation were kept fixed at 50 μm and 90%, respectively.

The powder bed was cured at 180 °C for 6 h to crosslink the polyethylene glycol (PEG) based binder and obtain the green specimens. These were then debinded (470 °C, 3 h, 2 °C min^{-1}) and presintered (1380 °C, 2 h, 2 °C min^{-1}) in a single thermal cycle in a chamber furnace (Lenton UAF 14/27, CARBOLITE GERO, UK) to remove the organic material and consolidate the parts. The debinding conditions for PEG were adopted from previous studies [27] and were confirmed after thermogravimetric analyses (TGA Q500, TA Instruments, US) of granulated powders with PEI in the 0–600 °C range in air. The components were finally sintered at 1700 °C for 1 h (Route 1 - Electric furnace, ATN 30/18, Nannetti S.r.l., Italy) and, for A30I2L and B30I2S samples only, at 1750 °C for 3 h (Route 2).

At each stage of the process, the geometry of the parts was measured with a digital calliper and the density was calculated by geometrical method. The internal porosity of the components was evaluated by mercury intrusion porosimetry (AutoPore IV 9500, Micromeritics Instrument Corporation, US) on samples from powders A30I2L and A30I2S, and observed by optical and scanning electron microscopy.

3. Results and discussion

3.1. Morphologic and colloidal characterisation of the raw materials

SEM images in Fig. 2 show the shape and the surface morphology of the studied particles. As can be seen from Fig. 2B, CT530SG powder seems to feature an ultrafine fraction combined with a coarser fraction (above 10 μm) constituted by platelets-like particles and aggregates. The CT1200SG and BITOSSI powders show a more homogeneous PSD$_V$ (Fig. 2A and C). These differences are highlighted also by the volume-granulometries in Fig. 3, which underline the distinction between monomodal (CT1200SG and BITOSSI) and bimodal (CT530SG) PSD$_V$. On one hand, the bimodality could be an advantage in terms of maximum packing of the powder, thus for the quality of the printed component [28,29]; on the other hand, the ultrafine fraction may require a larger amount of dispersant to stabilise the suspensions, since the size and SSA of the particles are normally correlated (Table 3) [30]. It should be noted that all curves display shoulders at smaller and larger diameters with respect to the main peaks: the nanometric fraction may not be relevant in terms of volume, thus not being highlighted in the PSD$_v$, however their specific surface is higher than that of the micrometric fraction. The unusual SSA of tested particles with mean sizes
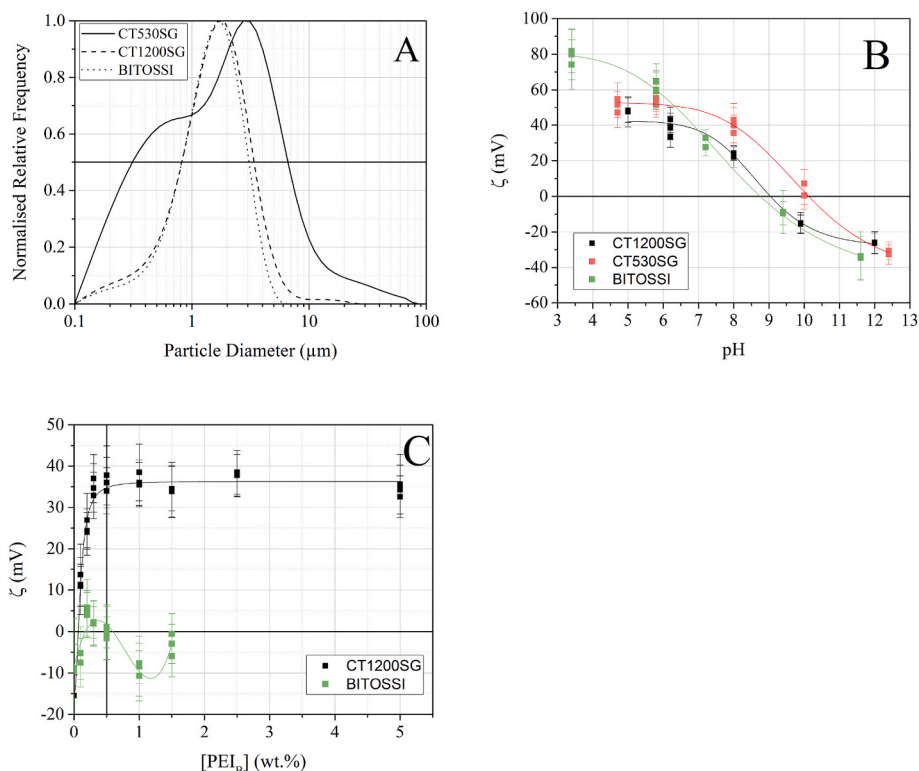
Fig. 3. A) Relative PSD$_V$ of the raw materials employed (Almatis CT1200SG – dashed; Almatis CT530SG – solid; BITOSSI – dotted), and ζ-potential values of diluted suspensions (1 gL^{-1}) of alumina powders at varying B) pH and C) PEI concentrations.

Table 3
$D_{10}/D_{50}/D_{90}$ from volume granulometry and SSA values from N$_2$-adsorption measurements of the three raw powders.

Powder	D_{10}	D_{50}	D_{90}	Type of PSD$_V$	SSA
	μm	μm	μm		m^2 g^{-1}
CT1200SG	0.6	1.7	3.7	monomodal	2.9
CT530SG	0.3	1.9	7.4	bimodal	5.4
BITOSSI	0.6	1.6	3.1	monomodal	2.7

close to 2 μm, determined by N$_2$-adsorption, confirm the influence of the ultrafine fraction on the average SSA of the three powders.

The results of isoelectric point (IEP) obtained from CT1200SG and BITOSSI powders (Fig. 3B) are coherent with the literature values of alumina in water at pH 8.5–9 (Fig. 3B) [31,32]. CT530SG has the IEP at pH ≥ 10, which could be due to the presence of a little amount of binder in the aggregates (slight mass lost of 0.25 wt% determined by DTA-TGA, e.g. top-right corner of Fig. 2B) of the coarser fraction as a result of a partial granulation process. Therefore, this material was not studied further to avoid difficulties in the study of the binders used to control the dispersion and binding mechanisms.

Fig. 3C shows the ζ-potential values after addition of PEI at different concentrations and pH ≥ 10, which was selected due to the correlated negative ζ potential as suitable condition for the stability optimisation with polycationic species. From Fig. 3C, only CT1200SG showed a transition to positive ζ-potential values, which stabilised at ~35 mV with [PEI] = 0.3 wt%. The BITOSSI sample, instead, had an initial increase at [PEI] = 0.3 wt%, and the values then stabilised close to neutral potential.

3.2. Granulation process and granules characterisation

The rheology of the PEI stabilised alumina suspensions was

evaluated to identify the maximum volume fraction to produce dense granules, associated with low enough viscosity for spray drying. As can be seen from Fig. 4A and B, both alumina suspensions feature a marked pseudoplastic behaviour with a shear thinning effect up to at least γ' = 1000 s^{-1} for Φ$_{vol}$ > 0.25. To obtain suitable viscosities for spray drying, the evolution of the viscosity at γ' = 100 s^{-1} with the volume fraction is plotted for both alumina suspensions stabilised with different PEI additions (Fig. 4C and D). The limit stands in 0.30 < Φ$_{vol}$ < 0.35 regardless of the PEI concentration in the case of CT1200SG (Fig. 4C), while the suspension of the BITOSSI powder featured a sharp reduction in viscosity when increasing [PEI] at 0.5 wt% (Fig. 4D). The low ζ-potential (positive only for [PEI] = 0.2 wt% and null for [PEI] = 0.5 wt%) promotes the effective steric stabilization of BITOSSI powder suspensions, that reduces the viscosity. The values collected at γ' = 100 s^{-1} from all the curves were fitted using the Krieger-Dougherty model (Eq. (1)): the model resulted in Φ$_{vol,max}$ = 0.48 ± 0.01 and Φ$_{vol,max}$ = 0.46 ± 0.01 for CT1200SG and BITOSSI, respectively.

As listed in Table 1, after the suspensions were stabilised and the solid content adjusted to obtain a suitable rheology (Fig. 5), different binders (PEG and PEI) and spray-drying conditions were tested with α-Al$_2$O$_3$ CT1200SG to achieve the successful granulation of the powder with an efficient process in terms of mass yield. The SEM images in Fig. 6A, B, 6C and 6D show that in all cases at least a granulated fraction was produced with an excellent shape regularity, as confirmed by the distribution curves of the particles according to their circularity (Fig. 6E). However, the amount of granulated materials and its average size vary in between the different processing conditions. In particular, samples A30I2L and A35G1L featured an improved regularity with most of the particles featuring a circularity above 0.8; instead, A30I2S and A35I2S display a large fraction of irregular particles, which were probably not aggregated to granules.

As known from literature, the morphology of the granulated material depends on multiple factors related to both the colloidal suspension and the spray-dryer configuration [33–35]. In this study, the effect of surface
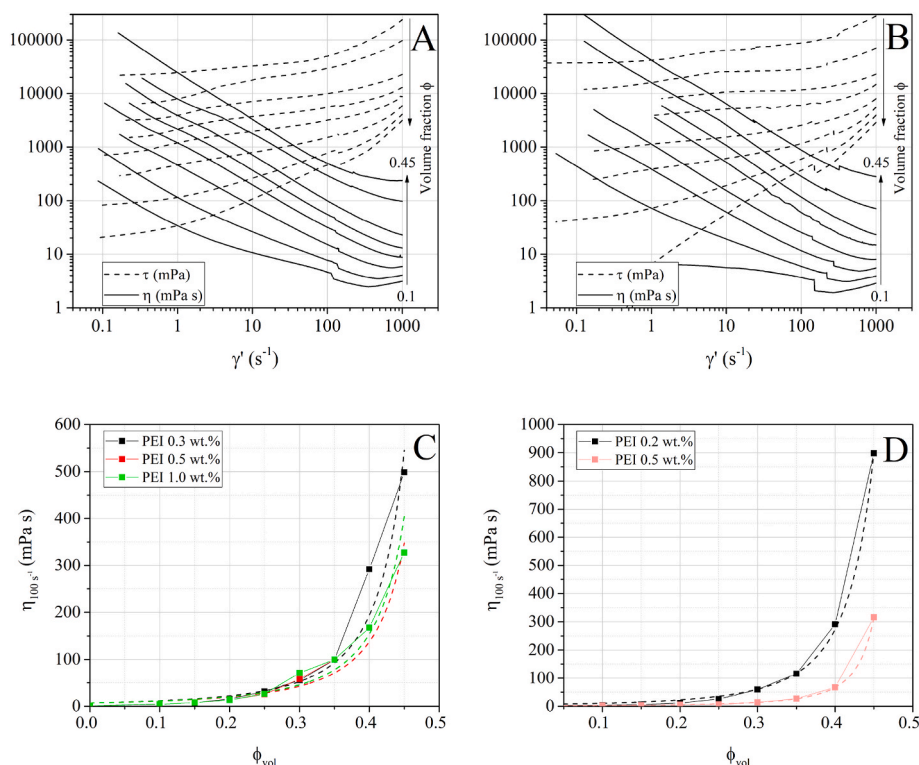
Fig. 4. Flow curves at increasing volume fraction for A) α-Al$_2$O$_3$ CT1200SG suspension with [PEI] = 0.3 wt% and B) α-Al$_2$O$_3$ BITOSSI suspension with [PEI] = 0.2 wt %; viscosity values at γ' = 100 s^{-1}, fitted according to Krieger-Dougherty model of C) α-Al$_2$O$_3$ CT1200SG suspension with [PEI] = 0.3/0.5/1.0 wt% and D) α-Al$_2$O$_3$ BITOSSI suspension with [PEI] = 0.2/0.5 wt%.
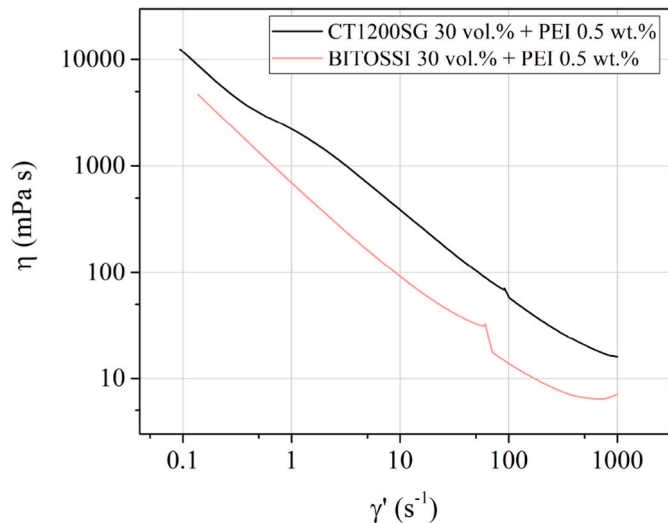

Fig. 5. Viscosity vs shear rate curves for the powder and dispersant combinations of choice for granulation.

tension, density and viscosity of the suspension due to its composition can be analysed from A30G2L/A30I2S/A35G1L/A35I2S results, where variations on the solid content and the amount and nature of the binder were considered. Instead, the influence of nozzle diameter and chamber temperature can be observed by comparing A30I2S to A30I2L and A30I2SHT, for suspensions prepared with a 30 wt% of solids and the addition of 0.5 wt% PEI as stabiliser and an extra amount of 2 wt% PEI as binder.

It should be noted that the volume- and number-based granulometric analyses tend to highlight different fractions of the PSD. At the

volumetric analysis the coarse fraction of particles is more relevant (Fig. 7A and B), while the number analysis allows to observe in detail differences in the ultrafine fraction (Fig. 7C and D).

Starting from the volumetric measurements in Fig. 7A, routes A30I2S and A30I2SHT feature a reduced sub-micron fraction and a final D$_{V10}$ > 1 μm, likely due to the presence of a sufficient number of granules. Those routes lead to granules of 15 μm of mean diameter and D$_{V90}$ of 50 and 40 μm, respectively, being A30I2S the PSD$_V$ with the largest granules due to the lower cyclone temperatures (205–140 °C) used if compare with A30I2SHT conditions (250–160 °C). The A30I2L, A30G2L, A35G1L and A35I2S conditions lead to a minimal variation of the fine fraction with respect to the as received α-Al$_2$O$_3$ CT1200SG powders. In A30G2L, A35G1L and A35I2S the formation of granules can be observed, A35I2S exhibiting a bimodal distribution. The number PSD$_N$ (Fig. 7C) shows the presence of an ultrafine fraction (<500 nm) in all granulated powders, while in the case of the raw material the correlated peak was less pronounced likely due to tendency to aggregate in absence of PEI stabiliser. In the 500 nm–10 μm range, the sample with the highest particles count is A30I2L, that shows a significant number of fine granules (below 2 μm). The case of BITOSSI powder granulation (B30I2S in Fig. 7B and D) is peculiar: the coarse (>10 μm) fraction is present as in A30I2S, however ultrafine (<500 nm) and a decent amount of fine (500 nm–10 μm) particles can be found too.

The only difference between the A30I2S and A30I2SHT routes is related to the temperature at the inlet of the granulator chamber, which in the second case is responsible for the formation of fine granules that seems to be lacking in A30I2S (see also Table 4). However, the main difference stands in the process yield, which was improved by >20% when employing T$_{inlet}$ = 250 °C. This can be explained by considering the faster dehydration of the droplets generated at the nozzle, which therefore do not stick to the chamber walls and flow freely in the collector. The nozzle diameter instead does not seem to have an influence on the yield, which is similar for A30I2S and A30I2L. A35I2S featured a reduced average size of the coarse fraction with respect to A30I2S and
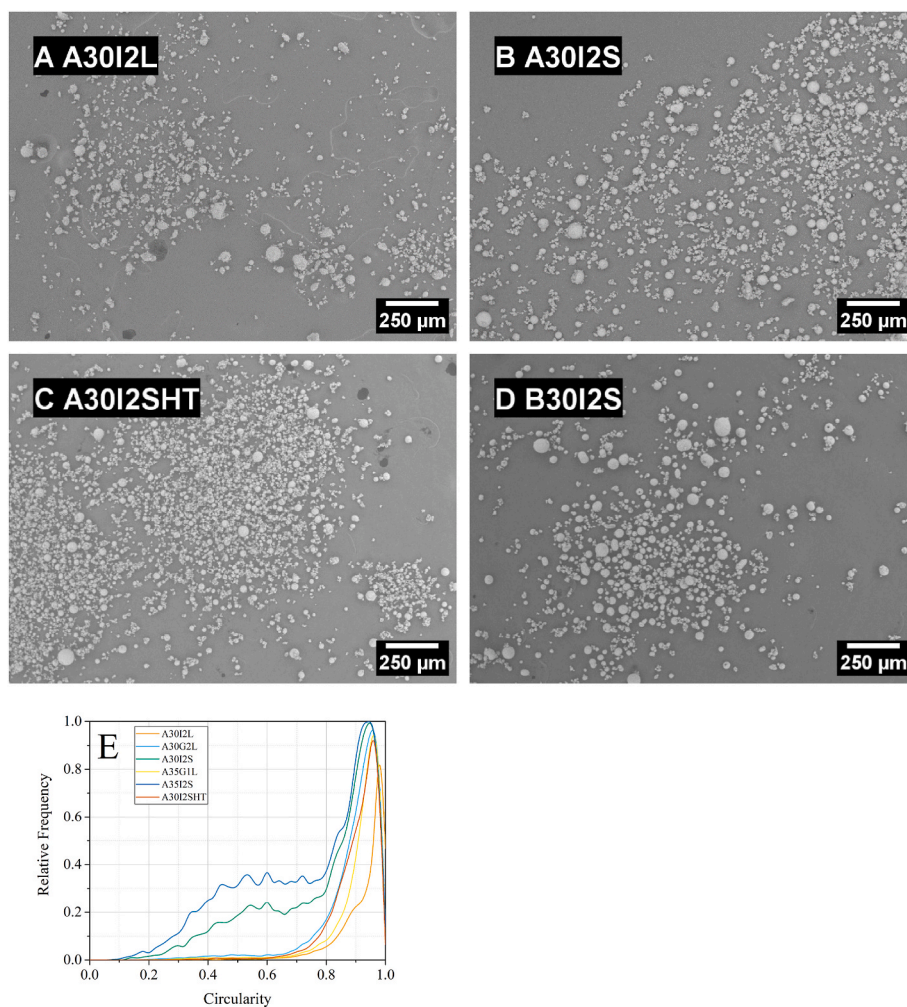
Fig. 6. SEM images of the A) A30I2L, B) A30I2S, C)A30I2SHT, and D) B30I2S granulated powders; E) Relative frequency curves of the circularity of the granulated powders.

A30I2SHT. In this case, the higher solid loading was responsible for the increased viscosity of the suspension, which likely generated smaller and more concentrated drops at the nozzles that broke in spherical droplets of reduced size [33,36].

A30G2L and A35G1L routes proved to be not feasible, regardless of their PSD. Indeed, more than half of the granulated material had to be manually detached from the wall chambers. The tendency to stick to the sides and form a sort of crust could be attributed to the presence of polyelectrolytes of opposite nature in the suspensions (anionic – PEG, cationic – PEI) which may have favoured the electrostatic interaction in between granules and prevented the free flowing of the material in the collector.

Finally, A30I2L differed from A30I2S only for the nozzle diameter. A larger diameter led to the formation of a bigger droplet at the nozzle, which probably were broken into a larger number of spherical drops generating a more consistent amount of fine granules. Similarly to A30I2S, the low inlet temperature combined with a reduced solid loading was responsible for a larger residual humidity in the droplets, which led to a higher risk of granules sticking to the chamber walls, thus to a reduced process yield.

The BITOSSI granulation (B30I2S) leads to the best results in terms of process yield (Table 4), which is drastically increased with respect the granulation of the CT1200SG powders under similar conditions (in process and suspension composition, A30I2S). The improvement is related to the suspension properties. It can be observed from Fig. 5 that the viscosity of the BITOSSI suspension is reduced with respect to the

CT1200SG powder suspension, which may have facilitated the flowing of the suspension within the nozzle feeder, thus avoiding material waste at this stage.

As mentioned above, meaningful quantitative analysis of the flowability of powders for binder jetting are challenging. The Hausner ratio may be a useful index, since it gives an indication of how well powder flow before and after applying compaction, but it has two flaws:

- the apparent density is solely dependent on the packing behaviour due to gravity, whose effect is less significant when dealing with low density and reduced size powder, due to the effect of electrostatic interactions acting among fine and ultrafine particles [18];
- the tap density is calculated after compaction of the powder and it should be representative of the maximum packing of the particles, however large overestimations could be induced by deformations and fragmentation of the granules, which do not occur during the powder bed formation phase of the printing process [21,29,37].

From Table 4, the largest densities were achieved by A30I2L, A30G2L and B30I2S for the apparent, and A30I2L, A30G2L and A35G1L for the tapped. The only correlation that seems to be highlighted is that between ρ_{tap} and the PSD, where a shift toward smaller diameters seems to be beneficial to packing by tapping. Overall, the only granulated powder that feature a clearly improved flowability from this analysis is B30I2S. However, the dispensing rate clearly indicate that the flowability from a hopper activated by ultrasound is enhanced also for
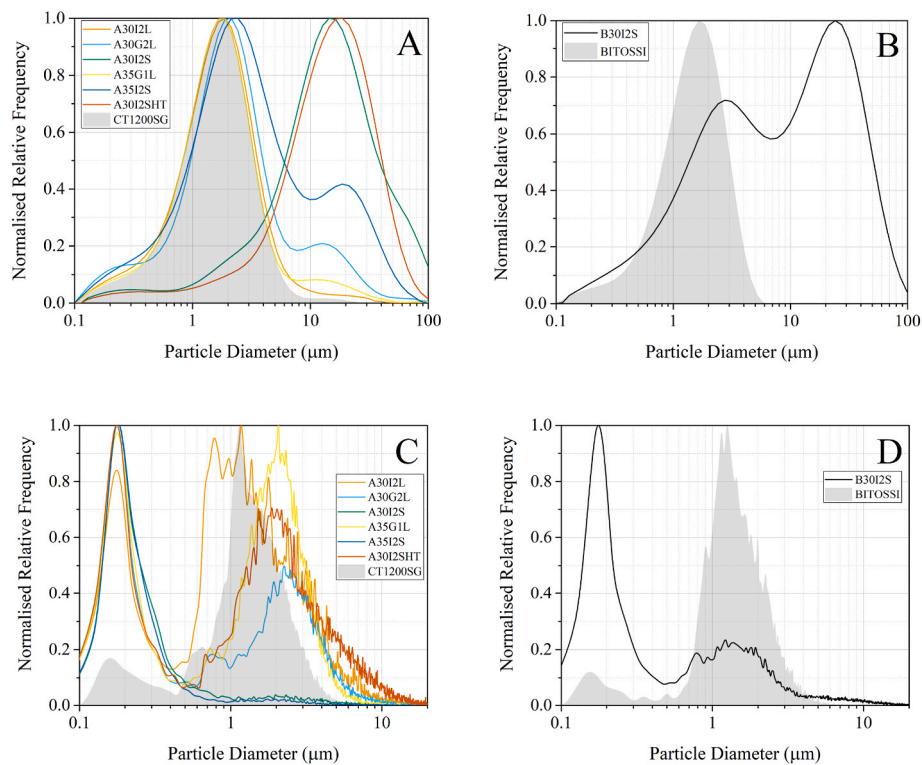
Fig. 7. Relative size distributions curves from PSD$_V$ (A,B) and PSD$_N$ (C,D) of the granulated powders and the starting powders (grey area) for A,C) Almatis CT1200SG and B,D) BITOSSI.

Table 4
Process yield, density, Hausner ratio, dispensing rate, volume- and number-based size distribution values of the granulated powders.

	Yield	ρ_{app}	ρ_{tap}	HR	Dispensing rate	Vol. Granulometry			Num. Granulometry		
						D$_{10}$	D$_{50}$	D$_{90}$	D$_{10}$	D$_{50}$	D$_{90}$
	%	%	%		mg cm^{-2} s^{-1}	μm	μm	μm	μm	μm	μm
A30I2L	64.7	23.5	31.3	1.33	96.3	0.6	1.8	4.2	0.7	2.3	6.6
A30G2L	82.1	27.1	34.8	1.28	1.3	0.6	2.2	11.3	0.8	2.8	6.1
A30I2S	65.3	22.2	27.7	1.25	6.8	3.0	15.0	50.4	<0.2	0.6	7.3
A35G1L	80.7	20.0	31.5	1.57	3.9	0.6	1.8	4.7	1.1	2.3	4.1
A35I2S	75.1	22.3	27.7	1.25	8.6	0.7	3.0	22.6	<0.2	0.3	6.4
A30I2SHT	88.1	20.1	26.0	1.29	4.9	3.8	15.8	40.3	1.3	3.3	9.6
B30I2S	92.3	25.9	27.8	1.08	36.2	1.1	9.1	42.8	0.2	1.9	10.2

*not calculated due to absent flow during measurement.

A30I2L, in addition to B30I2S.

In addition, A30G2L and A35G1L shows insufficient dispensing for the printing process, whereas the Hausner ratio did not underline such behaviour. This is likely due to their tendency at forming aggregates due to the presence of both a polyanion and a polycation in the granules which may generate attractive electrostatic interactions, and a relevant not-granulated fine fraction of particles prone to humidity-induced capillarity. Such aggregates are not influential when measuring the apparent and tapped density, but they are pivotal to the powder behaviour when the material must flow through a grid without the application of an external pressure. The results of the dispensing rates combined with the issues concerning the collection of the powders from the spray-dryer chamber led to the choice of excluding these powders, and PEG as binder, from the printing tests.

In conclusion, the deposition in our printing system with fine powders seems to benefit from a wide size distribution where granulated powders should be relevant in terms of volume (coarse fraction) and, even more, of number (fine fraction) to act positively on the flowing behaviour. Therefore, improvements should be expected by producing not a significant coarse fraction alone, but also a relevant number of particles with diameters ranging from the upper limit of the ultrafine size (500 nm) up to 10 μm.

3.3. Printed components characterisation

The average green density values of the components in Fig. 8A reflects both the degrees of packing measured by apparent density and the dispensing rates for the employed feedstocks (Table 4), which is to be expected because the powder bed formation does not feature any compaction mechanism as that of the tapped density tests. In all cases, the green densities exceed the values of the apparent one, which is due to the mechanism of powder bed formation: the layer-by-layer deposition promotes the material packing and prevents the formation of macropores within the body, which is more likely to occur when the powder is poured altogether [14,38]. The packing density of the green components influences on the geometrical accuracy as well, as can be seen in Fig. 8B. Overall, the building direction (Z) is the less accurate, which is to be expected given:
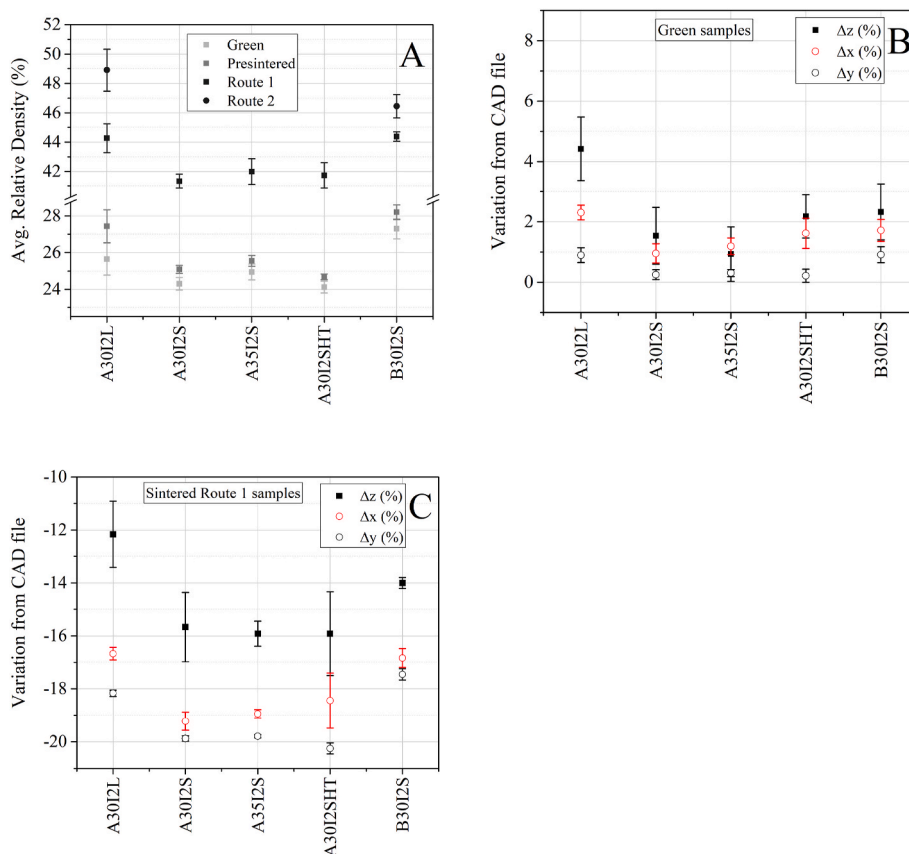
Fig. 8. A) Average relative density of the green, presintered at 1380 °C and sintered (route1-1700 °C and route2-1750 °C) specimens; B) Dimensional variations of the cured specimens (green) with respect to the CAD file; C) Dimensional variations of the sintered specimens (route 1–1700 °C) with respect to the CAD file. (For interpretation of the references to colour in this figure legend, the reader is referred to the Web version of this article.)
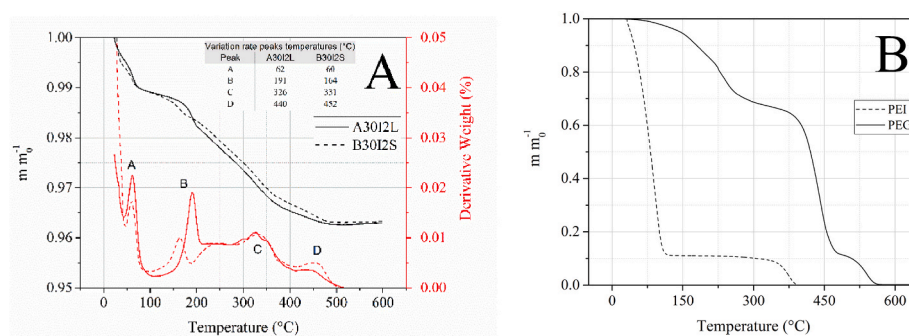

Fig. 9. Thermogravimetric analysis of: A) A30I2L and B30I2S granulated powders and B) polyethyleneimine (PEI) and polyethylene glycol (PEG).

1. The higher probability of trapping macropores at the interface of each layer, rather than within each layer, due to improper particles packing;
2. The possible localised oversaturation of binder on the highest region of each layer that can lead to the formation of additional spacing after curing, thus evaporation of the volatile solvents of the binder.

The accuracy on the planar direction (X, Y) is dependent on the lateral spreading of the binder in the first seconds after its deposition. In this case, the inaccuracies do not sum up at each layer as in the Z-direction, but only the largest one will contribute to the maximum size of the specimen in the X- or Y- directions, therefore a lower deviation from the designed size is to be expected.

It should be noted that the accuracy is expressed as a percentage of the samples dimension in the respective direction, thus the same deviation in absolute values results in a smaller relative variation on the larger size (Y-direction). Therefore, the only case in which the comparative variations in the three directions are not negligible is A30I2L, which features on average a +72 µm, +138 µm, +177 µm on the Y-, X- and Z-axis, respectively. The differences among the Y- and X-directions are likely due to the jetting mode of the binder droplets, which is beyond the scope of this study.

The presintering procedure leads to a slight increase in the average density of all components, producing binder-free pieces with a sufficient mechanical resistance to allow handling and placing in the sintering furnace. Complete debinding was confirmed for both PEG of the printer binder, as known from literature, and PEI from granulation (see Fig. 9A and B). The increase in density from green to presintered state confirms that minimal densification and shrinkage as occurred, otherwise the weight loss due to binder burnout would have led only to a density
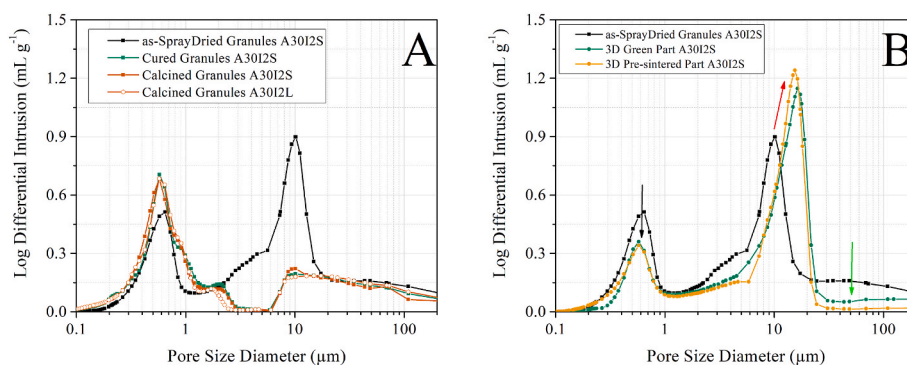
Fig. 10. Mercury Intrusion Porosimetry curves of A) as-spray dried, cured and calcined granules of A30I2S and A30I2L, and B) as-spray dried, cured and presintered 3D printed components of A30I2S.
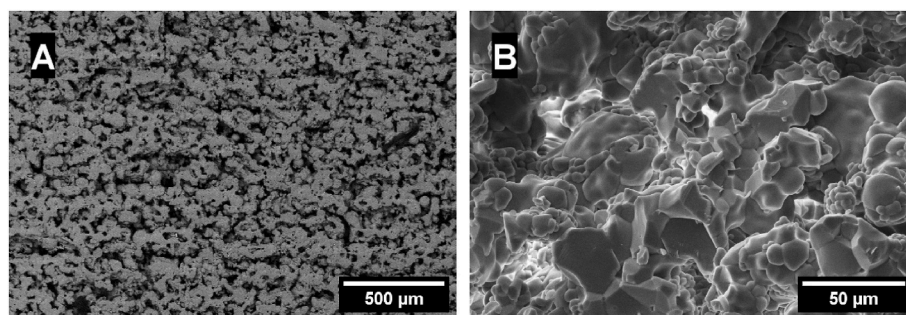

Fig. 11. SEM images of the cross section A30I2L sintered (route 2) specimens.

reduction.

Route 1 (1700 °C, 1 h) sintering produces an evident densification of the specimen with an increase of the relative density of about +16/17% for all the considered feedstocks, with A30I2L and B30I2S providing the best results. Further densification is achieved with route 2 sintering (1750 °C, 3 h), in particular for A30I2L powder that achieves an average final density close to 50%. Fig. 8C highlights that the sintered dimensions with respect to those of the CAD file varies differently in the three directions, which is of importance when generating the requested design. Nonetheless these variations reflect the excess sizes along the three directions observed in the green components. Therefore, the actual linear shrinkages in the three directions occurs to a more similar degree, in particular for specimen A30I2L. It should be noted that the linear shrinkage along the building direction is always lower than along the planar direction due to the excess porosity being confined mainly to the interlayer region, as already observed in other studies [39].

Mercury intrusion porosimetry (Fig. 10A and B) underlines that there are three levels on characteristic macropores sizes, ranging: $d < 1$ μm, 1 μm $< d < 20$ μm and $d > 20$ μm. The granules display all types of porosity, coherently with the particles size distributions observed above. Indeed, granules feature the small porosity compatible with the particles that constitutes them, a medium porosity likely generated by aggregation of unbound particles on the surface of granules, and a residual large porosity that can be attributed to macroaggregates of unbound particles. These latter aggregates are not resistant, since they are not actually bound together by polymers, so the correlated large porosity almost disappears after powder bed formation (green arrow in Fig. 10B): they are broken apart during deposition from the powder hopper and spreading by the roller. However, it should be noted that green samples medium porosity increases both in terms of cumulative volume and average size (red arrow in Fig. 10B). This is due to the addition of interlayer porosity during printing, as reported in literature [20,40–42], and not due to granules aggregates, which almost disappear after thermal treatments, as can be seen from the cured and calcined curves in

Fig. 10A. Finally, aggregates removal and granules filling with PEG after imbibition of the printer binder seem to be responsible for small pores reduction (black arrow in Fig. 10B). The overall cumulative volume decreases from granules to green samples due to aggregates breaking and polymer filling, and from green to presintered and sintered due to pore-filling effect from volume diffusive mechanisms. SEM imaging (Fig. 11) of the sintered (route2) A30I2L specimens confirms the observations made on porosity. Indeed, almost complete densification of the granules is achieved (Fig. 11B), but residual porosity is still large, in particular in the interlayer regions, which can be clearly noted within the microstructure (Fig. 11A). This confirms that the presence of small/medium porosity in the powder bed, due to absence of a compaction mechanism during material deposition, is the main factor preventing full densification.

4. Conclusions

This study shows a systematic approach towards the production of fine ready-to-print powders for binder jetting. Three α-Al$_2$O$_3$ powders were analysed and successfully dispersed by employing a cationic polyelectrolyte generating an electro-steric effect. Then, granulation by spray drying was performed for two of them and several combinations of suspension composition and granulating conditions were tested to assess the effect of each factor on the final properties of the granules and to determine the optimal set of parameters to produce granules suitable for binder jetting. Finally, the selected fine and spherical granulated powders were employed in the printing process and their behaviour during the shaping and consolidation phases was characterised.

The presence of a multimodal particle size distribution with a numerically relevant fraction of micrometric granules is fundamental to improve the flowability of the feedstock during printing, whereas increasing the average granules diameter alone is not sufficient in case of a residual large sub-micron size fraction. As expected, the flowability is beneficial to powder bed packing, thus to green and sintered density.

Spray-drying granulation was successful in producing a feedstock that could be easily deposited during printing starting from ultrafine feedstocks with limited flowability. Further densification by thermal treatment alone proved to be challenging, however density can be increased by slurry infiltration as observed in literature [22,43]. In this perspective, the preparation of a stable suspension with an optimal rheology is a dual advantage: can be employed for granulation and, on the other hand, for post-processing after sintering.

Funding

Declaration of competing interest

The authors declare that they have no known competing financial interests or personal relationships that could have appeared to influence the work reported in this paper.

Acknowledgements

References

[1] J.C. Wang, H. Dommati, S.J. Hsieh, Review of additive manufacturing methods for high-performance ceramic materials, Int. J. Adv. Manuf. Technol. 103 (2019) 2627–2647, https://doi.org/10.1007/s00170-019-03669-3.

[2] Z. Chen, Z. Li, J. Li, C. Liu, C. Lao, Y. Fu, C. Liu, Y. Li, P. Wang, Y. He, 3D printing of ceramics: a review, J. Eur. Ceram. Soc. 39 (2019) 661–687, https://doi.org/10.1016/j.jeurceramsoc.2018.11.013.

[3] J. wei Cai, B. cheng Zhang, M. hang Zhang, Y. jie Wen, X. hui Qu, Indirect 3D printed ceramic: a literature review, J. Cent. South Univ. 28 (2021) 983–1002, https://doi.org/10.1007/s11771-021-4674-1.

[4] Y. Lakhdar, C. Tuck, J. Binner, A. Terry, R. Goodridge, Additive manufacturing of advanced ceramic materials, Prog. Mater. Sci. 116 (2021), 100736, https://doi.org/10.1016/j.pmatsci.2020.100736.

[5] H. Curto, A. Thuault, F. Jean, M. Violier, V. Dupont, J.C. Hornez, A. Leriche, Coupling additive manufacturing and microwave sintering: a fast processing route of alumina ceramics, J. Eur. Ceram. Soc. 40 (2020) 2548–2554, https://doi.org/10.1016/j.jeurceramsoc.2019.11.009.

[6] Y. Lu, Z. Mei, J. Zhang, S. Gao, X. Yang, B. Dong, L. Yue, H. Yu, Flexural strength and Weibull analysis of Y-TZP fabricated by stereolithographic additive manufacturing and subtractive manufacturing, J. Eur. Ceram. Soc. 40 (2020) 826–834, https://doi.org/10.1016/j.jeurceramsoc.2019.10.058.

[7] H. Li, Y. Liu, Y. Liu, K. Hu, Z. Lu, J. Liang, Investigating the relation between debinding atmosphere and mechanical properties of stereolithography-based three-dimensional printed Al2O3 ceramic, Proc. Inst. Mech. Eng. Part B J. Eng. Manuf. 234 (2020) 1686–1694, https://doi.org/10.1177/0954405420937855.

[8] M. Orlovská, Z. Chlup, Bača, M. Janek, M. Kitzmantel, Fracture and mechanical properties of lightweight alumina ceramics prepared by fused filament fabrication, J. Eur. Ceram. Soc. 40 (2020) 4837–4843, https://doi.org/10.1016/j.jeurceramsoc.2020.02.026.

[9] A. Eguiluz, A. Ferrández-Montero, J. Yus, A.J. Sanchez-Herencia, B. Ferrari, Dispersion of Ni nanoparticles into Ti(C,N) colloidal filaments for 3D printing by FFF, Open Ceram 5 (2021), 100064, https://doi.org/10.1016/j.oceram.2021.100064.

[10] M. Kumar, V. Sharma, Additive manufacturing techniques for the fabrication of tissue engineering scaffolds: a review, Rapid Prototyp. J. 27 (2021) 1230–1272, https://doi.org/10.1108/RPJ-01-2021-0011.

[11] F. Abdeljawad, D.S. Bolintineanu, A. Cook, H. Brown-Shaklee, C. DiAntonio, D. Kammler, A. Roach, Sintering processes in direct ink write additive manufacturing: a mesoscopic modeling approach, Acta Mater. 169 (2019) 60–75, https://doi.org/10.1016/j.actamat.2019.01.011.

[12] I.S. Elizarova, L. Vandeperre, E. Saiz, Conformable green bodies: plastic forming of robocasted advanced ceramics, J. Eur. Ceram. Soc. 40 (2020) 552–557, https://doi.org/10.1016/j.jeurceramsoc.2019.10.010.

[13] P. Miranda, E. Saiz, K. Gryn, A.P. Tomsia, Sintering and robocasting of β-tricalcium phosphate scaffolds for orthopaedic applications, Acta Biomater. 2 (2006) 457–466, https://doi.org/10.1016/j.actbio.2006.02.004.

[14] M. Mariani, R. Beltrami, P. Brusa, C. Galassi, R. Ardito, N. Lecis, 3D printing of fine alumina powders by binder jetting, J. Eur. Ceram. Soc. 41 (2021) 5307–5315, https://doi.org/10.1016/j.jeurceramsoc.2021.04.006.

[15] A. Zocca, P. Lima, J. Günster, LSD-based 3D printing of alumina ceramics, J. Ceram. Sci. Technol. 8 (2017) 141–148, https://doi.org/10.4416/JCST2016-00103.

[16] W. Du, X. Ren, Z. Pei, C. Ma, Ceramic binder jetting additive manufacturing: a literature review on density, J. Manuf. Sci. Eng. 142 (2020), https://doi.org/10.1115/1.4046248.

[17] S. Cao, F. Xie, X. He, C. Zhang, M. Wu, Postprocessing study for the controllable structures of ceramic green parts realized by a flexible binder jetting printing (BJP) solution, Adv. Mater. Sci. Eng. 2020 (2020) 1–17, https://doi.org/10.1155/2020/3865752.

[18] S. Diener, A. Zocca, J. Günster, Literature Review: methods for achieving high powder bed densities in ceramic powder bed based additive manufacturing, Open Ceram 8 (2021), 100191, https://doi.org/10.1016/j.oceram.2021.100191.

[19] I. Baesso, D. Karl, A. Spitzer, A. Gurlo, J. Günster, A. Zocca, Characterization of powder flow behavior for additive manufacturing, Addit. Manuf. 47 (2021), 102250, https://doi.org/10.1016/j.addma.2021.102250.

[20] M. Mariani, R. Beltrami, E. Migliori, L. Cangini, E. Mercadelli, C. Baldisserri, C. Galassi, N. Lecis, Additive manufacturing of lead-free KNN by binder jetting, J. Eur. Ceram. Soc. (2022), https://doi.org/10.1016/j.jeurceramsoc.2022.05.075.

[21] G. Miao, W. Du, M. Moghadasi, Z. Pei, C. Ma, Ceramic binder jetting additive manufacturing: effects of granulation on properties of feedstock powder and printed and sintered parts, Addit. Manuf. 36 (2020), 101542, https://doi.org/10.1016/j.addma.2020.101542.

[22] A.L. Qirong Chen, Enrique Juste, Marie Lasgorceix, Fabrice Petit, Binder jetting process with ceramic powders: influence of powder properties and printing parameters, Open Ceram 9 (2021), 135907, https://doi.org/10.1016/j.oceram.2022.100218.

[23] I.M. Krieger, T.J. Dougherty, A mechanism for non-Newtonian flow in suspensions of rigid spheres, Trans. Soc. Rheol. 3 (1959) 137–152, https://doi.org/10.1122/1.548848.

[24] J.J. Stickel, R.L. Powell, Fluid mechanics and rheology of dense suspensions, Annu. Rev. Fluid Mech. 37 (2005) 129–149, https://doi.org/10.1146/annurev.fluid.36.050802.122132.

[25] Q. Li, V. Rudolph, B. Weigl, A. Earl, Interparticle van der Waals force in powder flowability and compactibility, Int. J. Pharm. 280 (2004) 77–93, https://doi.org/10.1016/j.ijpharm.2004.05.001.

[26] D. Oropeza, R. Roberts, A.J. Hart, A rapid development workflow for binder inks for additive manufacturing with application to polymer and reactive binder ink formulation, J. Manuf. Process. 73 (2022) 471–482, https://doi.org/10.1016/j.jmapro.2021.10.068.

[27] N. Lecis, M. Mariani, R. Beltrami, L. Emanuelli, R. Casati, M. Vedani, A. Molinari, Effects of process parameters, debinding and sintering on the microstructure of 316L stainless steel produced by binder jetting, Mater. Sci. Eng. A. 828 (2021), 142108, https://doi.org/10.1016/j.msea.2021.142108.

[28] R.M. German, Prediction of sintered density for bimodal powder mixtures, Metall. Trans. A. 23 (1992) 1455–1465, https://doi.org/10.1007/BF02647329.

[29] W. Du, J. Roa, J. Hong, Y. Liu, Z. Pei, C. Ma, Binder jetting additive manufacturing: effect of particle size distribution on density, J. Manuf. Sci. Eng. Trans. ASME. 143 (2021), https://doi.org/10.1115/1.4050306.

[30] G. Tari, J.M.F.F. Ferreira, A.T. Fonseca, O. Lyckfeldt, Influence of particle size distribution on colloidal processing of alumina, J. Eur. Ceram. Soc. 18 (1998) 249–253, https://doi.org/10.1016/s0955-2219(97)00113-1.

[31] G.A. Parks, The isoelectric points of solid oxides, solid hydroxides, and aqueous hydroxo complex systems, Chem. Rev. 65 (1965) 177–198, https://doi.org/10.1021/cr60234a002.

[32] M. Kosmulski, The pH-dependent surface charging and the points of zero charge, J. Colloid Interface Sci. 253 (2002) 77–87, https://doi.org/10.1006/jcis.2002.8490.

[33] A. Stunda-Zujeva, Z. Irbe, L. Berzina-Cimdina, Controlling the morphology of ceramic and composite powders obtained via spray drying – a review, Ceram. Int. 43 (2017) 11543–11551, https://doi.org/10.1016/j.ceramint.2017.05.023.

[34] I.M. Cotabarren, D. Bertín, M. Razuc, M.V. Ramírez-Rigo, J. Piña, Modelling of the spray drying process for particle design, Chem. Eng. Res. Des. 132 (2018) 1091–1104, https://doi.org/10.1016/j.cherd.2018.01.012.

[35] A.B.D. Nandiyanto, K. Okuyama, Progress in developing spray-drying methods for the production of controlled morphology particles: from the nanometer to submicrometer size ranges, Adv. Powder Technol. 22 (2011) 1–19, https://doi.org/10.1016/j.apt.2010.09.011.

[36] A. Tsetsekou, C. Agrafiotis, I. Leon, A. Milias, Optimization of the rheological properties of alumina slurries for ceramic processing applications Part II: spray-drying, J. Eur. Ceram. Soc. 21 (2001) 493–506, https://doi.org/10.1016/S0955-2219(00)00232-6.

[37] M. Li, G. Miao, M. Moghadasi, Z. Pei, C. Ma, Ceramic binder jetting additive manufacturing: relationships among powder properties, feed region density, and powder bed density, Ceram. Int. 47 (2021) 25147–25151, https://doi.org/10.1016/j.ceramint.2021.05.175.

[38] D. Oropeza, R.W. Penny, D. Gilbert, A.J. Hart, Mechanized spreading of ceramic powder layers for additive manufacturing characterized by transmission x-ray imaging: influence of powder feedstock and spreading parameters on powder layer density, Powder Technol. 398 (2022), 117053, https://doi.org/10.1016/j.powtec.2021.117053.

[39] M. Zago, N.F.M. Lecis, M. Vedani, I. Cristofolini, Dimensional and geometrical precision of parts produced by binder jetting process as affected by the anisotropic shrinkage on sintering, Addit. Manuf. 43 (2021), 102007, https://doi.org/10.1016/j.addma.2021.102007.

[40] M. Mariani, I. Goncharov, D. Mariani, G. Pietro De Gaudenzi, A. Popovich, N. Lecis, M. Vedani, Mechanical and microstructural characterization of WC-Co consolidated by binder jetting additive manufacturing, Int. J. Refract. Met. Hard Mater. 100 (2021), 105639, https://doi.org/10.1016/j.ijrmhm.2021.105639.

[41] G. Miao, M. Moghadasi, W. Du, Z. Pei, C. Ma, Experimental investigation on the effect of roller traverse and rotation speeds on ceramic binder jetting additive manufacturing, J. Manuf. Process. 79 (2022) 887–894, https://doi.org/10.1016/J.JMAPRO.2022.05.039.

[42] M. Moghadasi, W. Du, M. Li, Z. Pei, C. Ma, Ceramic binder jetting additive manufacturing: effects of particle size on feedstock powder and final part properties, Ceram. Int. 46 (2020) 16966–16972, https://doi.org/10.1016/j.ceramint.2020.03.280.

[43] J. Vogt, H. Friedrich, M. Stepanyan, C. Eckardt, M. Lam, D. Lau, B. Chen, R. Shan, J. Chan, Improved green and sintered density of alumina parts fabricated by binder jetting and subsequent slurry infiltration, Prog. Addit. Manuf. (2021) 1–11, https://doi.org/10.1007/s40964-021-00222-1.